



HAL
open science

Geology of the Neruda quadrangle (H13), Mercury

Benjamin Man, David A Rothery, Matthew R Balme, Susan J Conway, Jack Wright, David L Pegg, Annie R Lennox, Salvatore Buoninfante

► **To cite this version:**

Benjamin Man, David A Rothery, Matthew R Balme, Susan J Conway, Jack Wright, et al.. Geology of the Neruda quadrangle (H13), Mercury. *Journal of Maps*, 2023, 19 (1), pp.2256353. 10.1080/17445647.2023.2256353 . hal-04262548

HAL Id: hal-04262548

<https://hal.science/hal-04262548v1>

Submitted on 30 Oct 2023

HAL is a multi-disciplinary open access archive for the deposit and dissemination of scientific research documents, whether they are published or not. The documents may come from teaching and research institutions in France or abroad, or from public or private research centers.

L'archive ouverte pluridisciplinaire **HAL**, est destinée au dépôt et à la diffusion de documents scientifiques de niveau recherche, publiés ou non, émanant des établissements d'enseignement et de recherche français ou étrangers, des laboratoires publics ou privés.



Distributed under a Creative Commons Attribution 4.0 International License



Geology of the Neruda quadrangle (H13), Mercury

Benjamin Man, David A. Rothery, Matthew R. Balme, Susan J. Conway, Jack Wright, David L. Pegg, Annie R. Lennox & Salvatore Buoninfante

To cite this article: Benjamin Man, David A. Rothery, Matthew R. Balme, Susan J. Conway, Jack Wright, David L. Pegg, Annie R. Lennox & Salvatore Buoninfante (2023) Geology of the Neruda quadrangle (H13), Mercury, Journal of Maps, 19:1, 2256353, DOI: [10.1080/17445647.2023.2256353](https://doi.org/10.1080/17445647.2023.2256353)

To link to this article: <https://doi.org/10.1080/17445647.2023.2256353>



© 2023 The Author(s). Published by Informa UK Limited, trading as Taylor & Francis Group on behalf of Journal of Maps



[View supplementary material](#)



Published online: 14 Sep 2023.



[Submit your article to this journal](#)



Article views: 289











[View related articles](#)



[View Crossmark data](#)



Geology of the Neruda quadrangle (H13), Mercury

Benjamin Man ^a, David A. Rothery ^a, Matthew R. Balme ^a, Susan J. Conway ^b, Jack Wright ^c,
David L. Pegg ^a, Annie R. Lennox ^a and Salvatore Buoninfante ^{d,e}

^aSchool of Physical Sciences, The Open University, Milton Keynes, UK; ^bLaboratoire de Planétologie et Geosciences, Nantes Université, Université d'Angers, Le Mans Université, Nantes, France; ^cEuropean Space Agency (ESA), European Space Astronomy Centre (ESAC), Madrid, Spain; ^dDipartimento di Scienze della Terra, dell'Ambiente e delle Risorse, Università degli Studi di Napoli 'Federico II', Naples, Italy; ^eIstituto di Astrofisica e Planetologia Spaziali (IAPS), INAF, Rome, Italy

ABSTRACT

We present the first geological map of the Neruda Quadrangle (H13), Mercury. H13 is in Mercury's southern hemisphere between latitudes 22.5°S–65°S, and longitudes 90°E–180° covering a total area of just under 5 million km², equivalent to 6.5% of the planet's surface. Map digitisation was carried out at scales between 1:300,000 and 1:700,000 for final presentation at 1:3,000,000, from end-of-mission data products from NASA's MESSENGER mission. We distinguish three main photogeologic plains units: intercrater, intermediate, and smooth plains. We also distinguish all craters and their materials ≥ 20 km in diameter based on their degradation state. We have completed two versions of the map, one using a three-class crater degradation scheme and one using a five-class crater degradation scheme. In addition, specific geological units were charted for the Rembrandt impact basin. This map has been constructed to provide context and targets for the ESA-JAXA BepiColombo mission to Mercury.

ARTICLE HISTORY

Received 15 June 2023
Revised 23 August 2023
Accepted 31 August 2023

KEYWORDS

Mercury; geological map;
Neruda quadrangle; H13

1. Introduction

Although known since antiquity, the earliest recorded attempts to map Mercury's surface date from the early 1800s but could not produce geologically meaningful results. This changed when Mariner 10 completed three flybys of the planet between 1974 and 1975, and the surface of Mercury was revealed for the first time. Mariner 10 imaged ~40–45% of the planet's surface and several authors produced geological maps using those data (DeHon et al., 1981; Grolier & Boyce, 1984; Guest & Greeley, 1983; King & Scott, 1990; McGill & King, 1983; Schaber & McCauley, 1980; Spudis & Guest, 1988; Spudis & Prosser, 1984; Strom et al., 1990; Trask & Dzurisin, 1984; Trask & Guest, 1975). In 1978, Mercury was divided into 15 mapping quadrangles informally named after prominent surface features that had image coverage and telescopic albedo features for areas with no image coverage (Davies et al., 1978). Only the very eastern edge of the H13 quadrangle (170°E–180°) was imaged by Mariner 10 and this was included in the map of the H12 (Michelangelo) quadrangle (Spudis & Prosser, 1984).

MESSENGER (MErcury Surface, Space ENvironment, GEochemistry, and Ranging), the second and most recent spacecraft to visit Mercury, was able to image the entire planet whilst in orbit between 2011




and 2015 (Solomon & Anderson, 2018). This enabled production of the first global geological map at a scale of 1:15M (Kinczyk et al., 2019; Prockter et al., 2016). Consequently, H13 was renamed after the prominent Neruda crater instead of the now obsolete albedo feature Solitudo Persephones.

The improved spatial resolution achieved by MESSENGER has allowed for mapping at a larger scale than the 1:5M mapping undertaken with Mariner 10 data. At the time of writing, 7 out of 15 MESSENGER-based quadrangle maps have been published at a scale of 1:3M (Galluzzi et al., 2016; Giacomini et al., 2022; Guzzetta et al., 2017; Malliband et al., 2023; Mancinelli et al., 2016; Pegg et al., 2021b; Wright et al., 2019). Here we present the first geological map of H13, Neruda (Main Map – see Supplementary information).

2. Data

2.1. Basemaps

We used a suite of data products with differing incidence angles to obtain information in places otherwise obscured by shadows. These data products were produced by the MESSENGER team who used the Mercury Dual Imaging System (MDIS) wide-angle camera (WAC) and narrow-angle camera (NAC) data (Denevi et al., 2018; Hawkins et al., 2007).

CONTACT Benjamin Man  ben.man@open.ac.uk  School of Physical Sciences, The Open University, Milton Keynes, MK7 6AA, UK
 Supplemental data for this article can be accessed online at <https://doi.org/10.1080/17445647.2023.2256353>.

© 2023 The Author(s). Published by Informa UK Limited, trading as Taylor & Francis Group on behalf of Journal of Maps

This is an Open Access article distributed under the terms of the Creative Commons Attribution License (<http://creativecommons.org/licenses/by/4.0/>), which permits unrestricted use, distribution, and reproduction in any medium, provided the original work is properly cited. The terms on which this article has been published allow the posting of the Accepted Manuscript in a repository by the author(s) or with their consent.

2.1.1. Map projected basemap reduced data record (BDR)

The primary basemap used was the end-of-mission monochrome v1 BDR mosaic and tiles composed of topographically controlled WAC and NAC images sampled to ~ 166 m/pixel (Figure 1(a)) (Murchie et al., 2017). These products of moderate incidence angle ($\sim 74^\circ$) highlight surface morphology.

2.1.2. Map-projected low incidence angle basemap reduced data record (LOI)

The v2 monochrome LOI mosaic (~ 166 m/pixel; Figure 1(b)) is composed of WAC and NAC images captured at low solar incidence angles ($\sim 45^\circ$) to emphasise albedo variations (Murchie et al., 2017), such as rays from young craters.

2.1.3. Map-projected high incidence East/West-illumination basemaps (HIE/HIW)

The v2 monochrome HIW (Figure 1(c)) and HIE (Figure 1(d)) products (~ 166 m/pixel) are composed of WAC and NAC images illuminated at high incidence angles ($\sim 78^\circ$) from the east and west respectively (Murchie et al., 2017). The high solar incidence angle of these products is extremely useful for identifying subtle topographic structures as well as revealing information in shadowed areas of the primary basemap.

2.1.4. Enhanced color global mosaic

The Enhanced Color Global Mosaic (665 m/pixel; Figure 1(e)) accentuates the colour differences on Mercury's surface (Denevi et al., 2018, Denevi, Seelos et al., 2016). The MESSENGER team made it using MDIS WAC images in the 430, 750 and 1000 nm bands. They applied principal component analysis placing the second principal component in the red channel, first principal component in the green channel and the 430/1000 ratio in the blue channel (Denevi et al., 2018). This product provides spectral context for morphological observations and is useful in the identification of deposits with a noticeable spectral response such as hollows (Blewett et al., 2011) and volcanic deposits (Goudge et al., 2014; Jozwiak et al., 2018; Kerber et al., 2011; Pegg et al., 2021a; Thomas et al., 2014a; Thomas & Rothery, 1984; Xiao et al., 2021).

2.1.5. Digital elevation model (DEM)

The v2 global DEM (665 m/pixel; Figure 1(f)) is derived from thousands of paired stereo images and controlled using MESSENGER's Mercury Laser Altimeter (Cavanaugh et al., 2007) elevation data (Becker et al., 2016). This product was critical in our identification and charting of tectonic structures and crater ejecta.

3. Methods

3.1. Projection

H13 is located in mid-southern latitudes and is centred on 135°E (Figure 2). We use a Lambert Conformal Conic (LCC) projected coordinate system with standard parallels of 30°S and 58°S , following previous mid-latitude MESSENGER-era quadrangle mappers (Galluzzi et al., 2016; Guzzetta et al., 2017; Mancinelli et al., 2016; Pegg et al., 2021b; Wright et al., 2019) (Figure 1) based on the 'Mercury 2015' geographic coordinate system (sphere radius = 2,439.4 km). The LCC projection preserves shapes and angles locally and has correct distance scale along the standard parallels, however, distances and areas are exaggerated outside the standard parallels and reduced between them (Kennedy & Kopp, 2004).

3.2. Scale

The map publication scale is 1:3M, the same as the published MESSENGER-era quadrangle maps. The drafting scale for a 1:3M map is suggested to be $\sim 1:750\text{k}$, $4\times$ the publication scale according to planetary mapping protocols by the United States Geological Survey (USGS) and German Aerospace Centre (DLR) (Hauber et al., 2020; Skinner et al., 2022). An alternative suggestion is that the drafting scale should be $2000\times$ the basemap resolution (Tobler, 1987). Considering the primary basemap has a spatial resolution of ~ 166 m/pixel, we calculate a drafting scale of $\sim 1:300\text{k}$. With both recommendations in mind, we predominantly mapped at a scale of 1:300k and up to 1:700k for some larger landforms.

3.3. Mapping process

We started mapping H13 in ArcMap 10.5.1 in 2019 and migrated to ArcGIS Pro in 2022. We started by making a project file with a dedicated geodatabase for the feature classes. Initially, we created four feature classes: (1) linear features (polylines); (2) contacts (polylines); (3) units (points) and (4) surface features (polygons). We began by digitising linear features, such as crater rims, then we mapped all tectonic structures. Next, we mapped crater material contacts while placing unit points and assigning crater degradation classifications to the attribute fields of those points. We then completed all remaining contacts for plains materials and their corresponding unit points. Finally, we digitised superficial units. We then generated polygons from the polylines of the geological 'contacts' and points of the 'units' feature classes to generate two versions (3 crater classes and 5 crater classes) of our map. ArcGIS's streaming tool was used for vertex placement of polylines and polygons with a streaming

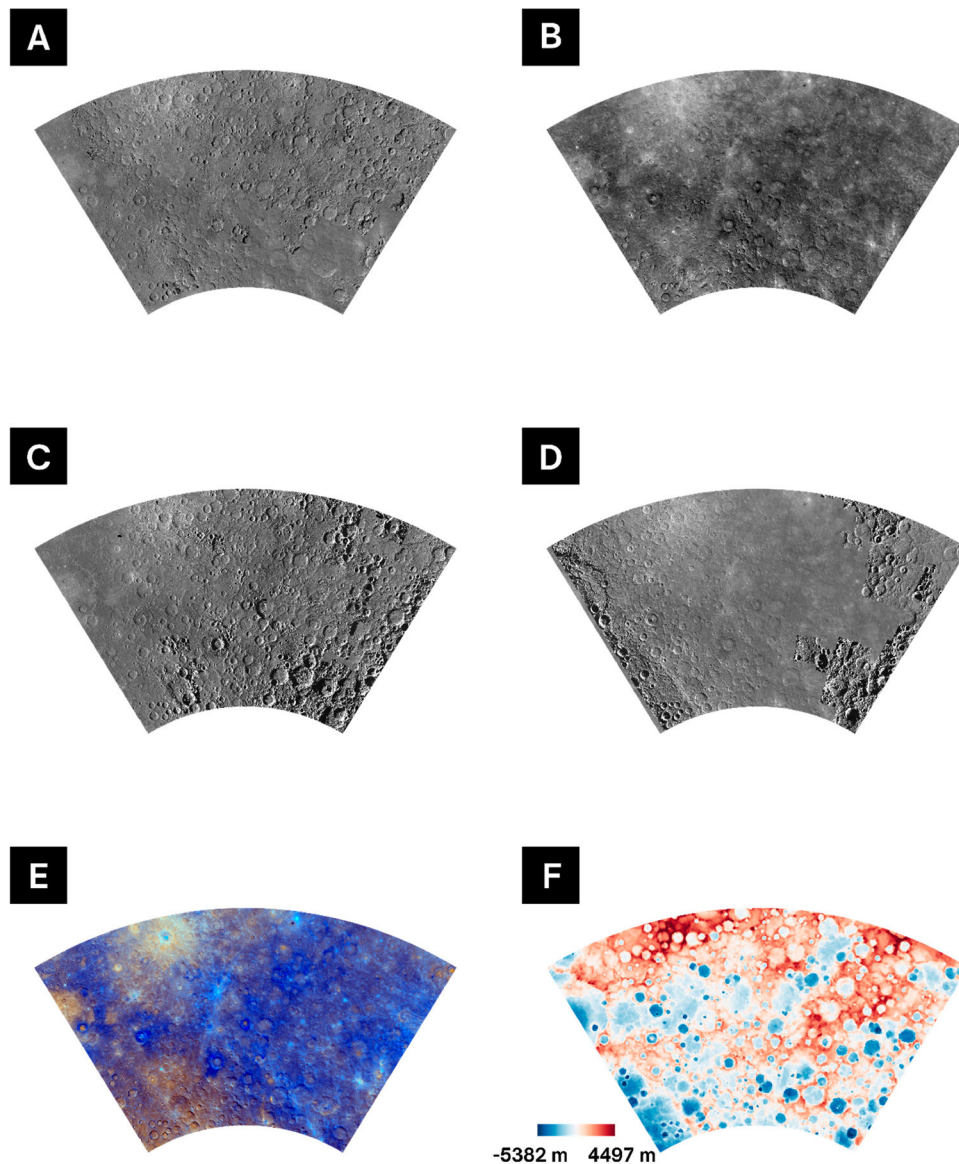


Figure 1. Data products used. A | Primary basemap, BDR Mosaic. B | LOI Mosaic. C | HIW tiles. D | HIE tiles. E | Enhanced Color Mosaic. F | DEM mosaic.

tolerance of 600 m. Unit symbology and definitions are consistent with previously published MESSENGER-era quadrangle maps with Rembrandt specific units after (Pegg et al., 2021b). Map symbology was finalised following the USGS planetary mapping protocols guidance for map symbology (Skinner et al., 2022) and then the map was labelled, and prepared for publication in ArcGIS Pro.

3.3.1. Linear features

The ‘linear features’ feature class contains all non-contact polylines including crater rims; ‘small’ (≥ 5 km and < 20 km in diameter); ‘large’ (≥ 20 km in diameter); and ‘buried-subdued’ (≥ 5 km in diameter). ‘Buried-subdued’ denotes crater rims that have been buried by plains materials or impact ejecta and/or have been otherwise heavily degraded. In addition to craters, we mapped the rims of irregularly shaped pits, interpreted as being related to volcanism (Jozwiak

et al., 2018; Pegg et al., 2021a; Rothery et al., 2014; Thomas et al., 2014b, 2014a). We also mapped wrinkle ridges in the same feature class. Wrinkle ridges are commonly found within smooth plains and smooth crater floor material and are believed to represent the surface manifestations of blind thrusts (Byrne et al., 2018; Klimczak et al., 2019).

3.3.2. Contacts

The boundary between units is termed a ‘contact’ and is traditionally identified by textural, compositional, structural or temporal differences between units (Howe, 1997). For our map we distinguish two types of stratigraphic contacts: ‘Certain’ and ‘Approximate’ with the designation indicating our confidence in the position of the contact location. ‘Certain’ contacts are where there is an obvious boundary that can be traced between geomorphic units. ‘Approximate’ contacts on the other hand demarcate boundaries that are

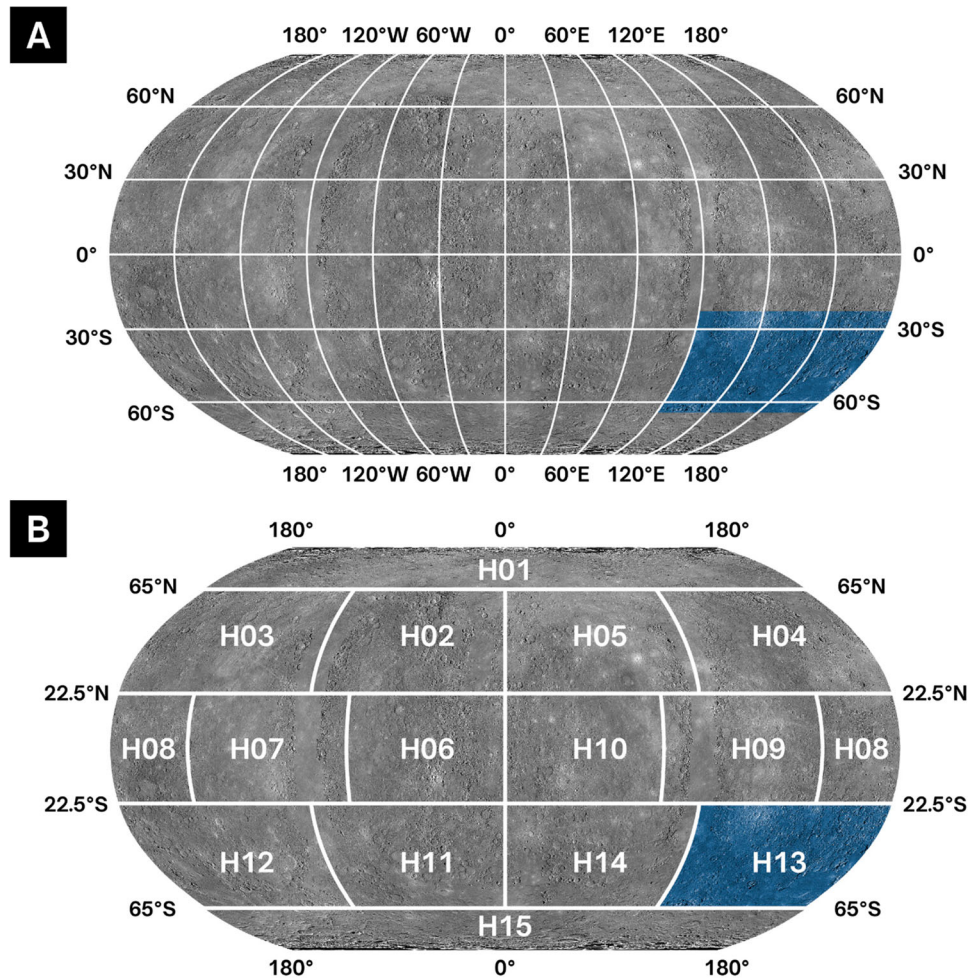


Figure 2. Location of the H13 Quadrangle. A | BDR Mosaic with graticule. B | BDR Mosaic with quadrangle outlines. H13 highlighted in blue.

either genuinely gradational or probably sharp but whose precise location cannot be identified.

A surface-breaking fault is a type of contact as displacement can result in different geomorphic units on either side of the fault. We include two types of thrust faults in the contacts feature class. ‘Thrust fault – certain’ is assigned to a structure with a clear break in slope where there is clear displacement. ‘Thrust fault – approximate’ is assigned for surface features that are shortening structures with less obvious breaks in slopes but with distinctive positive relief and/or the structure separates geomorphic units. We also include ‘Normal fault’ denoting faults that bound the graben structures found within the Rembrandt impact basin. Polylines were drawn along the leading edge of a structure where a sharp break in slope is discernible.

3.3.3. Units

The ‘units’ feature class consists of points with multiple attribute fields that when populated denote the geological unit in which the point is located. Units points were placed in mapped areas that were enclosed polylines, after contacts were mapped, and this feature

class was used in the construction of polygons for the final map product using ArcGIS Pro’s ‘Feature to Polygon’ tool. The units points were additionally used to generate and place a majority of the labels for the final map. Units points are not displayed on the map and were simply used in its construction.

3.3.4. Superficial units

Superficial units do not obscure the underlying major geomorphic units. They include: ‘rays’ of bright material ejected by impacts and still visible around some of the youngest, freshest craters (Braden & Robinson, 2013; Neish et al., 2013; Trask & Guest, 1975); ‘catenae’, chains of secondary craters (Fegan, 2018); ‘faculae’, bright, spectrally red aureoles with diffuse margins commonly centred on irregular pits and mostly interpreted as having been emplaced by explosive volcanism (Gillis-Davis et al., 2009; Kerber et al., 2011; Pegg et al., 2021a; Thomas et al., 2014b; Thomas & Rothery, 1984), and; fields of ‘hollows’, which are bright, spectrally blue irregularly-shaped depressions with flat floors and steep flanks (Blewett et al., 2011; Thomas et al., 2014c). All superficial features are represented by ornaments overlain on the

geological units so that no information is lost in the final map.

3.3.5. Reconciliation

We mapped a 5° overlap with all adjacent quadrangle maps to facilitate boundary matching, with a view to an eventual global geological map (Galluzzi et al., 2021).

3.4. Mapped units

3.4.1. Craters

With H13 being perhaps the most heavily cratered region on the planet (Denevi, Ernst, et al., 2016; Fassett et al., 2011), the craters in the quadrangle and their associated material make up a significant portion of the map. To understand the sequence of cratering and to compare the relative ages of craters not just on Mercury but with other planets, crater materials including rims, internal structures and ejecta are

classified according to their degradation state. It can be assumed that craters, including those not in contact with each other, of the same degradation state formed within the same span of geological time. While generally useful, this assumption breaks down in specific cases, such as where degradation is accelerated by burial with ejecta from a subsequent nearby large impactor, rather than background degradation processes.

Mapping at 1:5M scale, the Mariner 10-era mappers (DeHon et al., 1981; Guest & Greeley, 1983; King & Scott, 1990; McGill & King, 1983; Schaber & McCauley, 1980; Spudis & Prosser, 1984; Strom et al., 1990; Trask & Dzurisin, 1984) used a five-class crater degradation scheme. However, the first MESSENGER-era quadrangle mappers (Galluzzi et al., 2016; Guzzetta et al., 2017; Mancinelli et al., 2016) used a three-class crater degradation scheme (Figure 3) to avoid occasional apparent contradictions whereby ejecta from a crater classified as more degraded overlies ejecta from a crater classified as less degraded. Here

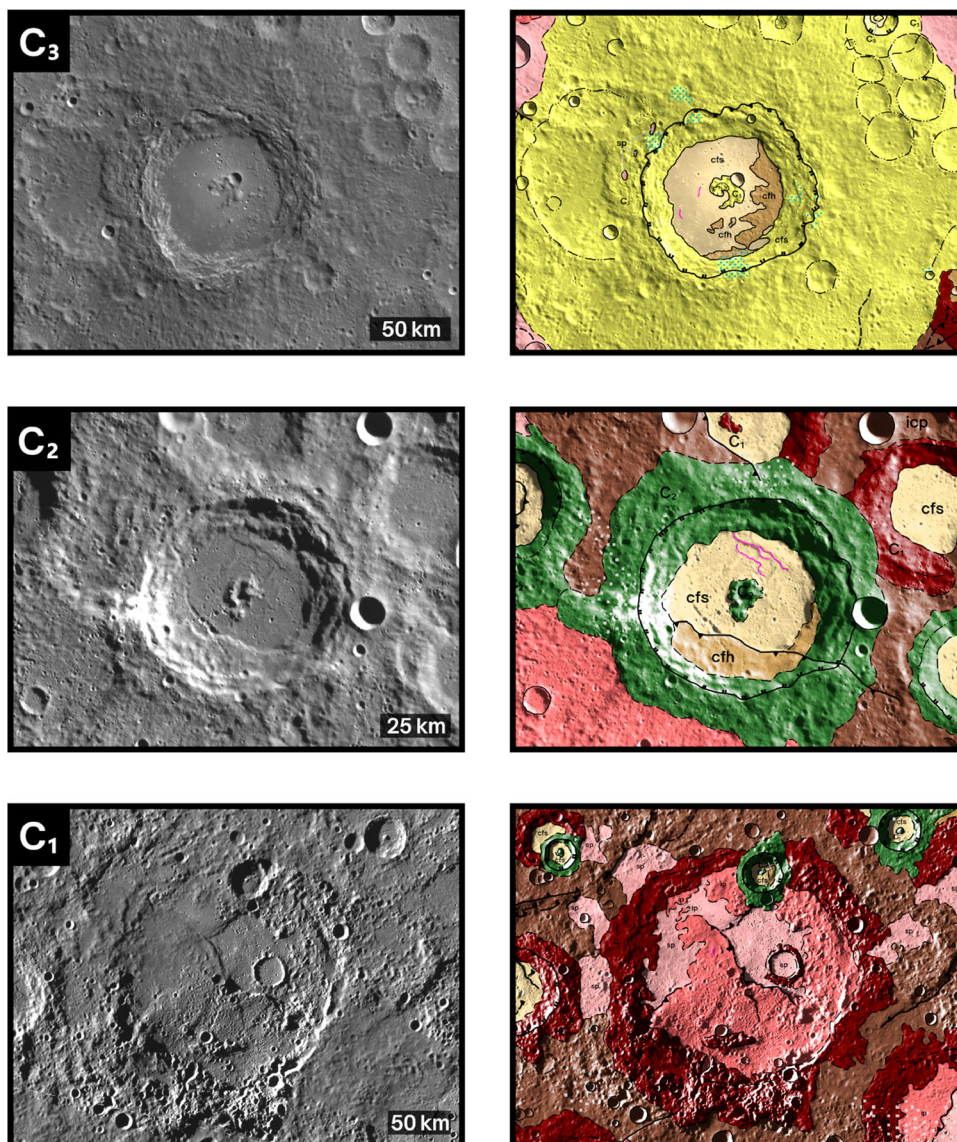


Figure 3. Three-class crater classification (C_3 – C_1). BDR Mosaic on the left and map interpretation on the right.

we follow several more recent MESSENGER-era mappers (Malliband et al., 2023; Pegg et al., 2021b; Wright et al., 2019) by simultaneously employing a five-class crater degradation scheme in parallel with the newer three-class scheme, on the grounds that the five-class scheme records more information and that this is intended to be morphostratigraphic rather than purely stratigraphic.

The three-class classification scheme (Figure 3) is given as: C_1 representing the oldest and most degraded, C_2 for craters intermediate in age and degradation state, and C_3 for the freshest craters with the crispest morphology. The five-class scheme (Figure 4) runs c_1 – c_5 (with lower case c) representing most degraded to freshest (and usually corresponding to oldest to youngest). The five-class crater

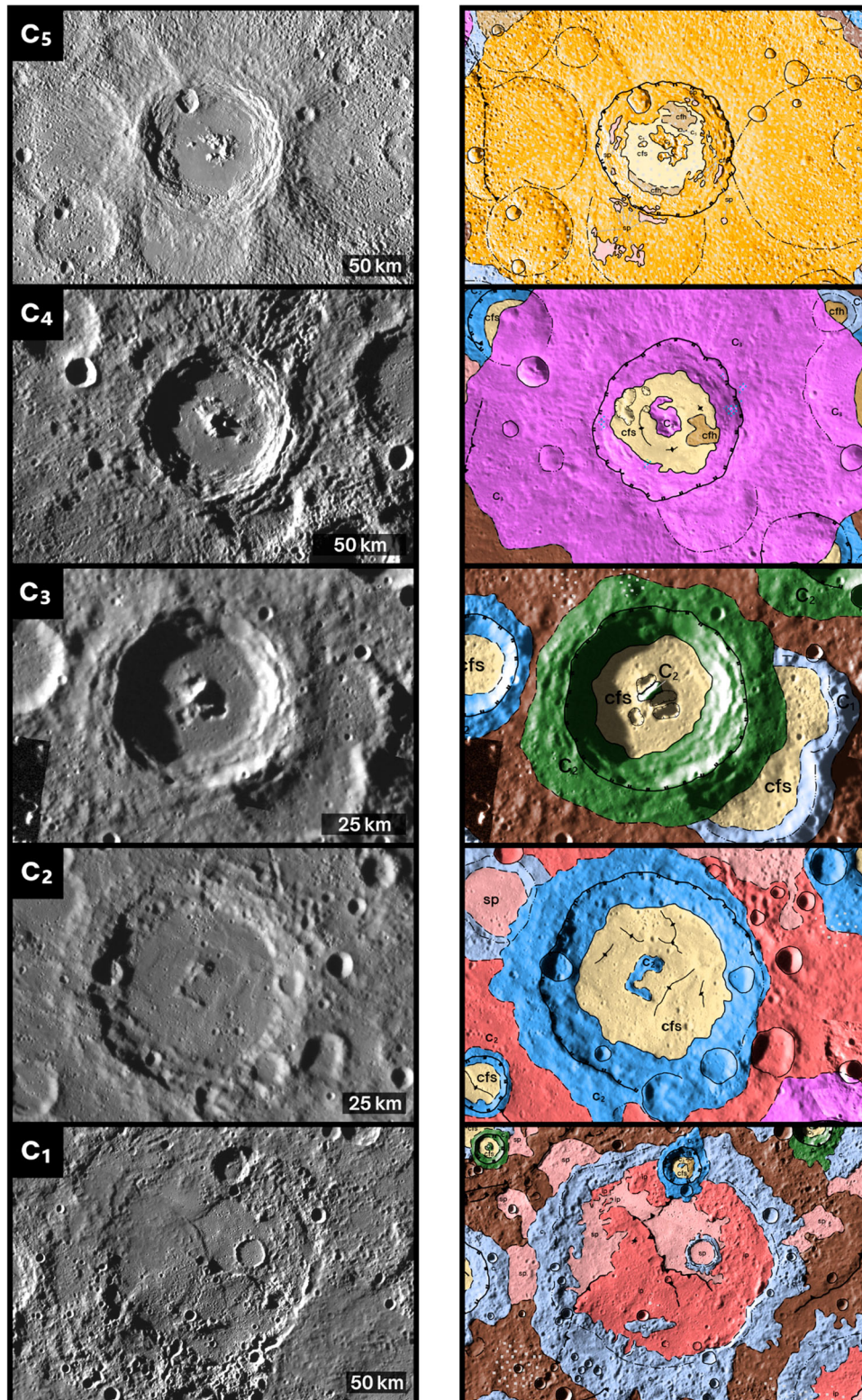


Figure 4. Five-class crater classification (c_5 – c_1). BDR Mosaic on the left and map interpretation on the right.

degradation scheme is not strictly stratigraphic in sequence, because crater degradation does not have to correspond to stratigraphic order (Kinczyk et al., 2020). Furthermore, not only do impactors of different sizes create craters of differing complexity but different sized craters degrade at different rates; smaller, less complex craters degrade faster than larger complex craters (Basilevsky & Vernadsky, 1976; Wood et al., 1977). Cognizant of this, and with a revised five-class crater degradation scheme available to us during our mapping (Kinczyk et al., 2020) we have produced both three-class and five-class versions of our map with all craters ≥ 20 km diameter classified. Below we outline the different schemes in detail.

3.4.1.1. Fresh craters (C_3 | c_5 , c_4). Pristine—well preserved craters with fresh, crisp rims and intact internal crater structures such as pronounced central peak/peak ring elements, upstanding wall terraces, textured ejecta blankets. For C_3 – three-class craters, rays may be present whilst for c_5 – five-class craters rays must be present (c_4 rays are absent) (Figure 3 and 4). Contacts between crater floor material and internal structures are sharp and well defined.

3.4.1.2. Degraded craters (C_2 | c_3 , c_2). Moderately degraded craters with obvious, but somewhat subdued, rims. Internal structures such as central peak/peak ring elements are subdued, and crater wall terraces are slumped or missing (Figure 3 and 4). Ejecta is discernible but distal ejecta can be rare (c_2) and lacks

radial texture (c_3). Contacts between crater floor material and internal structures are mostly sharp.

3.4.1.3. Heavily degraded craters (C_1 | c_2 , c_1). Craters with incomplete and/or significantly subdued and heavily degraded rims. No obvious internal structures whatsoever, only the largest craters may exhibit remnant central peaks/peak ring elements and any form of ejecta (Figure 3 and 4). C_1 and c_1 craters may have breached crater rims and floors flooded from external sources. Contacts between floor material and crater walls are often gradational and marked as approximate.

3.4.1.4. Smooth crater floor (cfs). Description: Sparsely cratered smooth material confined to the floors of craters (Figure 5).
Interpretation: In fresh craters (C_3 | c_5 , c_4) this is usually theorised to represent ponded impact melt that has solidified (Daniels & Neish, 2018; Malliband et al., 2023; Pegg et al., 2021b; Wright et al., 2019). In degraded craters it is possibly a combination of volcanic material and impact melt.

3.4.1.5. Hummocky crater floor (cfh). Description: Texturally rough or cratered material confined to within craters (Figure 5).
Interpretation: In fresh craters (C_3 | c_5 , c_4) hummocky material may represent original crater floor, free of impact melt. For degraded craters, hummocky crater floor material likely represents degraded

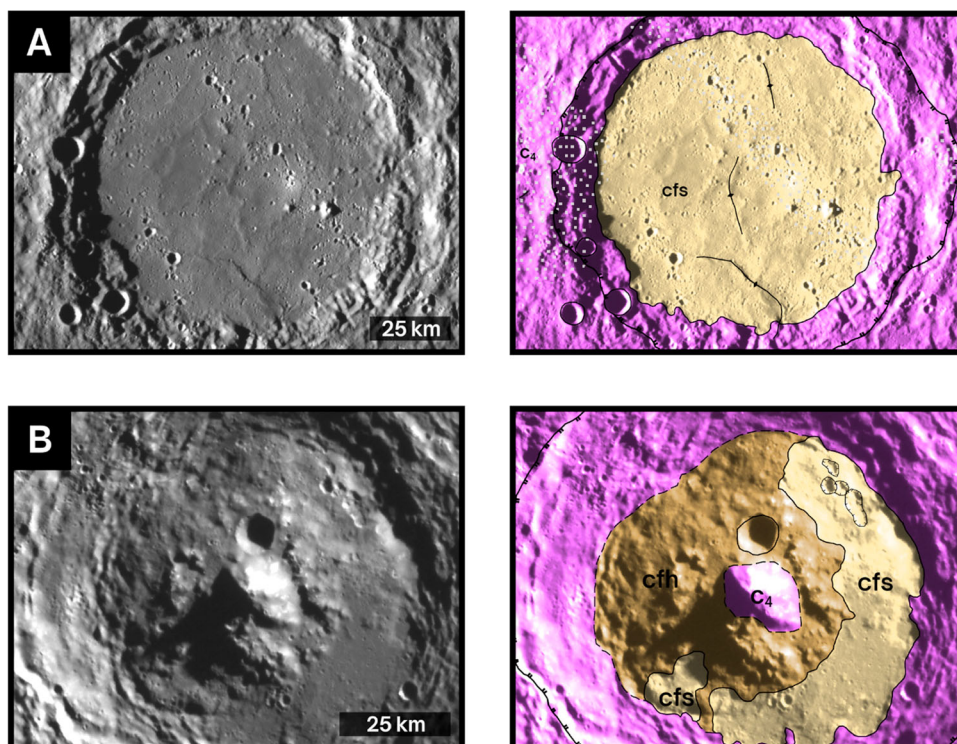


Figure 5. Crater floor materials. BDR Mosaic on the left hand side and map interpretation on the right hand side. Smooth crater floor material (cfs) and hummocky crater floor material (cfh).

internal structures and floor material inundated by distal ejecta from elsewhere.

3.4.2. Rembrandt units

The ~720 km Rembrandt impact basin straddles the H13 and H14 quadrangles and due to its size, basin-specific units are mappable (Figure 6) (Fassett et al., 2012; Whitten & Head, 2015). Following H14 quadrangle mapper

(Pegg et al., 2021b), we identify and include five Rembrandt-specific units after region specific mappers (Hynek et al., 2017; Semenzato et al., 2020).

3.4.2.1. Hummocky unit (Reh). Description: A texturally rough, undulating terrain of hills and depressions with a lower albedo than the interior smooth plains (Semenzato et al., 2020).

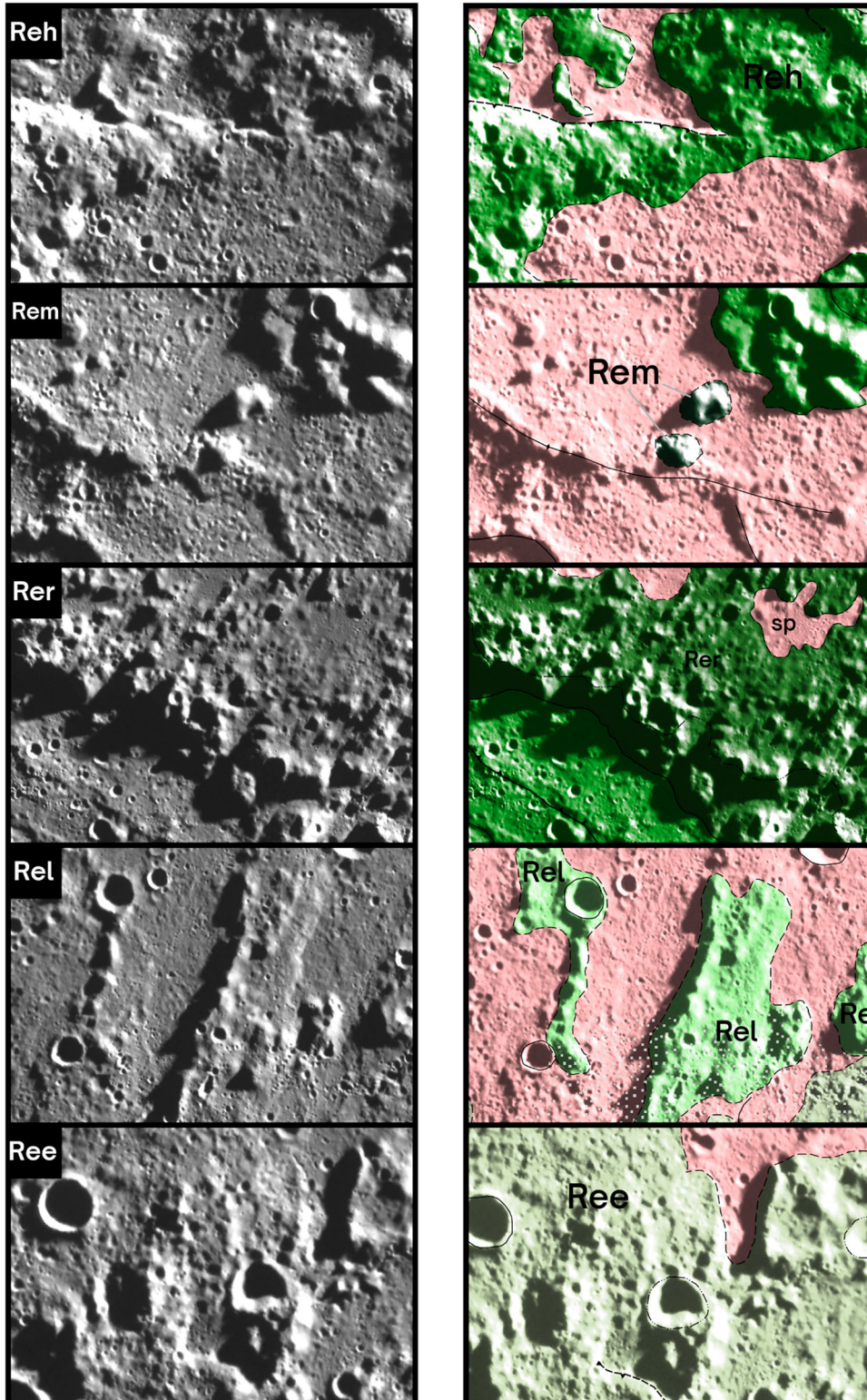


Figure 6. Rembrandt materials. BDR Mosaic on the left and map interpretation on the right. Rembrandt hummocky unit (Reh), Rembrandt massifs (Rem), Rembrandt rim (Rer), Rembrandt lineated ejecta (Rel) and Rembrandt ejecta (Ree).

Interpretation: This material is theorised to be part of the basin floor that has not been buried by lavas (Watters et al., 2009). The gradational boundary of the unit is consistent with lavas that have overlapped and embayed the upstanding hummocky unit, infilling depressions along the margins.

3.4.2.2. Massifs (Rem). Description: Blocky, isolated mountains within the Rembrandt impact basin.

Interpretation: These structures may represent isolated blocks of impact ejecta (Pegg et al., 2021b) or remnants of peak ring elements (Watters et al., 2009).

3.4.2.3. Rim (Rer). Description: A chain of massifs with significant relief, separating internal and external basin material.

Interpretation: These structures most likely represent the rim of the impact basin, similar to the Caloris Montes unit that rings the Caloris basin (Fassett et al., 2009; Pegg et al., 2021b).

3.4.2.4. Lineated ejecta (Rel). Description: Radially oriented material found in a series of ridges and troughs within the exterior smooth plains (Whitten & Head, 2015).

Interpretation: Interpreted as ejecta scour (in the case of the troughs) or deposited ridges of material radial to the rim of the impact basin (Whitten & Head, 2015). This unit is equivalent to the Van Eyck formation of the Caloris Basin (Fassett et al., 2009; Watters et al., 2009).

3.4.2.5. Ejecta (Ree). Description: Material found draped over terrain and infilling craters exterior to Rembrandt. The material is texturally hummocky and discontinuous.

Interpretation: Interpreted as ejecta that formed instantaneously after the Rembrandt impact event and basin formation.

3.5. Plains units

3.5.1. Intercrater plains (icp)

Description: A heavily cratered, highly textured unit (Figure 7). First identified by (Trask & Guest, 1975), intercrater plains are described as ‘level to gently rolling ground between and around large craters and basins’. Recognised as the most widespread geomorphic unit on the planet (Kinczyk et al., 2019; Strom et al., 1975), intercrater plains characteristically have a high density of superposing craters 5–15 km in diameter (Leake, 1981; Strom, 1977; Trask & Guest, 1975). Superposing craters however are not limited to 5–15 km but can be of all sizes and degradation classes. Spectrally, the intercrater plains are not associated with a definitive colour and can be spectrally highly variable.

Interpretation: Intercrater plains are theorised to be volcanic plains that have been extensively reworked, possibly predating the end of the Late Heavy Bombardment of the inner solar system (Strom et al., 1975; Trask & Guest, 1975). Given the density of superposing craters, the unit is likely to include a substantial quantity of reworked impact melt and ejecta.

3.5.2. Smooth plains (sp)

Description: Expanses of mostly flat, texturally smooth material with few superposing craters (Figure 7). Craters that superpose smooth plains are typically morphologically fresh with distinguishable ejecta blankets and sharp contacts. In H13, example areas of smooth plains are the interior and exterior plains of the Rembrandt impact basin. Spectrally, smooth plains are typically relatively red however, there is variation; for example the interior and exterior plains of the Rembrandt basin (Whitten & Head, 2015). Often in smooth plains are buried craters that are identifiable by wrinkle ridges demarcating an underlying crater rim. Wrinkle ridges unrelated to buried craters are also common throughout smooth plains. Small patches of smooth plains are found within other units such as infilling crater chains, perched on crater walls and ejecta or in partially fault-bounded or purely topographic depressions.

Interpretation: Expanses of smooth plains are interpreted as effusive volcanic material; lava flows that have not been heavily degraded (Byrne et al., 2016; Denevi et al., 2013, 2009; Thomas & Rothery, 1984; Whitten & Head, 2015). Isolated patches of smooth plains may represent ponded impact melt (Malliband et al., 2023; Pegg et al., 2021b; Wright et al., 2019).

3.5.3. Intermediate plains (ip)

Description: Expanses of material that are transitional in surface roughness between smooth and intercrater plains (Figure 7), with a density of superposing craters in-between that of smooth and intercrater plains (Galluzzi et al., 2016; Spudis & Prosser, 1984). In the case of H13, intermediate plains almost always have an ‘approximate’ boundary contact due to the gradational change from either smooth or intercrater plains into the unit. Intermediate plains exhibit a mantled appearance with many small isolated and interconnected small patches of smoother material alongside hummocky, upstanding mounds and ridges. Spectrally, the intermediate plains exhibit similar colour responses to intercrater plains however, some smoother patches appear brighter and redder, comparable to smooth plains.

Interpretation: This unit is interpreted as smooth plains material that has partially or thinly covered the older intercrater plains unit. The depressions were likely infilled and therefore became smooth, whereas components such as crater rims and ejecta

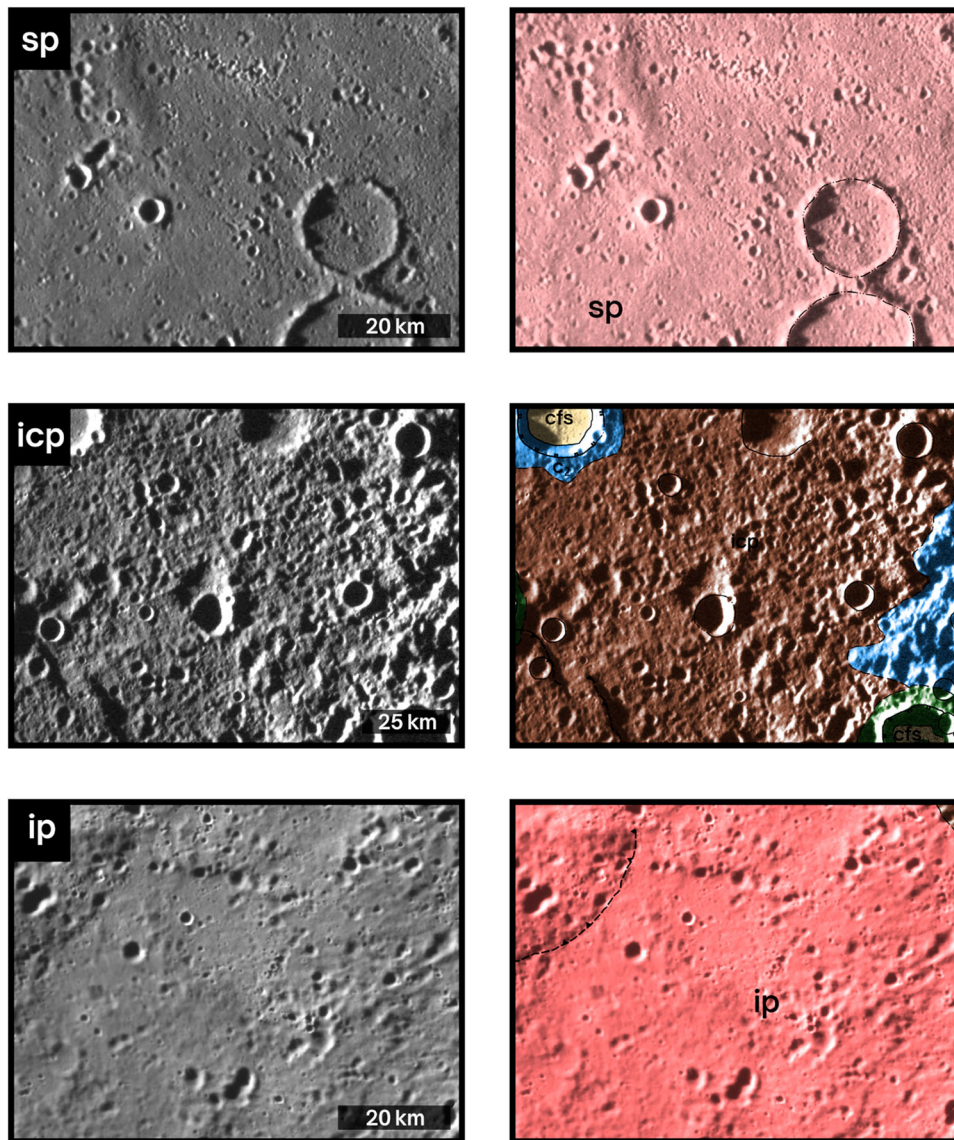


Figure 7. Plains materials. BDR Mosaic on the left side and map interpretation on the right side. Smooth plains (sp), intercrater plains (icp) and intermediate plains (ip).

may have only partially been covered, resulting in the aforementioned upstanding mounds and ridges. The inclusion of intermediate plains in our map follows previous MESSENGER-era quadrangle mappers to be comparable and equable for a future global map. It is important to note, however that elsewhere on Mercury, intermediate plains have been interpreted as plains units that are intermediate in age between intercrater plains and smooth plains (Galluzzi et al., 2016; Giacomini et al., 2022; Guzzetta et al., 2017; Maliband et al., 2023; Pegg et al., 2021b) and as a result, our correlation of map units allows for this.

4. Correlation of map units

Our stratigraphic columns (Figure 8) display the geological history of the mapped units for the H13 quadrangle for both three-class and five-class crater degradation schemes. The crater ages follow (Galluzzi et al., 2016) for the three-class version and (Spudis &

Guest, 1988) with amendments after (Banks et al., 2017; Ernst et al., 2017) for the five-class version. The plains materials are based on absolute model age estimates; for intercrater plains (Marchi et al., 2013; Whitten et al., 2014), and for smooth plains (Byrne et al., 2016).

5. Summary

Using the end-of-mission MESSENGER data products, we have produced the first geological map of the Neruda quadrangle (H13) of Mercury. The map was produced for publication at a scale of 1:3 M as part of the series of quadrangle maps that together will constitute a global geological map of the planet. This map provides for the first time geological context within the H13 quadrangle to be used by ESA-JAXA's BepiColombo mission to Mercury. The map shows that crater materials dominate the surface of H13. Smooth and intermediate plains are most common

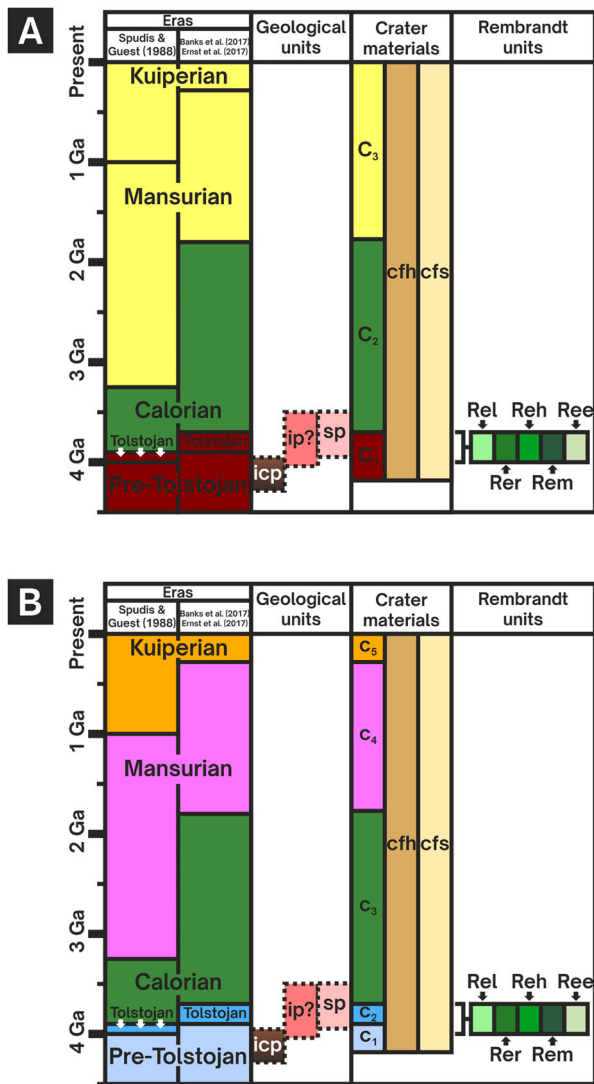


Figure 8. Correlation of map units. A | Three-class crater classification scheme. B | Five-class crater classification scheme.

in the west of the map, particularly interior and exterior to the Rembrandt impact basin. Intercrater plains are found amongst the high density of craters and are most abundant to the east of the quadrangle.

Software

We used ESRI ArcMap 10.5.1 and ArcGIS Pro 2.9.5 Geographic Information System software to produce the map. Basemaps were processed using USGS ISIS3 software. The final map sheets were put together in ArcGIS Pro 2.9.5 and CoreDRAW X6.

Acknowledgements

Gratitude is given to the UK Research and Innovation (UKRI) Science and Technology Facilities Council (STFC) and the Open University's Strategic Research Area in Space for making this research possible. Thanks are also given to GMAP (Geologic Mapping of Planetary Bodies) formerly PLANMAP (PLANetary

MAPping Project) for guidance and resources that helped with this work. SJC is grateful for the support of the French Space Agency, CNES for her BepiColombo related work. JW acknowledges support from the European Space Agency (ESA) as an ESA Research Fellow received during the write-up of this work. SB received funding from the Italian Space Agency (ASI) under ASI-INAF agreement 2017-47-H.0.

Disclosure statement

No potential conflict of interest was reported by the author(s).

Funding

This work was supported by European Space Agency; Istituto Nazionale di Astrofisica; The Open University; Centre National d'Études Spatiales; Science and Technology Facilities Council.

Data availability statement

All basemap data are publicly available from NASA's Planetary Data System (<https://pds-imaging.jpl.nasa.gov/portal/>). Digital copies of the map, constituent shapefiles and base-map raster can be found here: (10.21954/ou.rd.23386808).

ORCID

Benjamin Man <http://orcid.org/0000-0001-9056-6072>
 David A. Rothery <http://orcid.org/0000-0002-9077-3167>
 Matthew R. Balme <http://orcid.org/0000-0001-5871-7475>
 Susan J. Conway <http://orcid.org/0000-0002-0577-2312>
 Jack Wright <http://orcid.org/0000-0003-0481-0863>
 David L. Pegg <http://orcid.org/0000-0002-4468-8359>
 Annie R. Lennox <http://orcid.org/0009-0003-9305-6512>
 Salvatore Buoninfante <http://orcid.org/0000-0003-2596-9267>

References

- Banks, M. E., Xiao, Z., Braden, S. E., Barlow, N. G., Chapman, C. R., Fassett, C. I., & Marchi, S. S. (2017). Revised constraints on absolute age limits for Mercury's Kuiperian and Mansurian stratigraphic systems. *Journal of Geophysical Research: Planets*, 122(5), 1010–1020. <https://doi.org/10.1002/2016JE005254>
- Basilevsky, A. T., & Vernadsky, V. I. (1976). On the rate of evolution of small lunar craters.
- Becker, K. J., Robinson, M. S., Becker, T. L., Weller, L. A., Edmundson, K. L., Neumann, G. A., Perry, M. E., & Solomon, S. C. (2016). First Global Digital Elevation Model of Mercury. *Lunar and Planetary Science Conference*, 1–2. 2016LPI....47.2959B
- Blewett, D. T., Chabot, N. L., Denevi, B. W., Ernst, C. M., Head, J. W., Izenberg, N. R., Murchie, S. L., Solomon, S. C., Nittler, L. R., McCoy, T. J., Xiao, Z., Baker, D. M. H., Fassett, C. I., Braden, S. E., Oberst, J., Scholten, F., Preusker, F., & Hurwitz, D. M. (2011). Hollows on Mercury: MESSENGER evidence for geologically recent volatile-related activity. *Science*, 333(6051), 1856–1859. <https://doi.org/10.1126/science.1211681>

- Braden, S. E., & Robinson, M. S. (2013). Relative rates of optical maturation of regolith on Mercury and the Moon. *Journal of Geophysical Research: Planets*, 118(9), 1903–1914. <https://doi.org/10.1002/jgre.20143>
- Byrne, P. K., Klimczak, C., & Celâl Şengör, A. M. (2018). The tectonic character of Mercury. In S. C. Solomon, L. R. Nittler, & B. J. Anderson (Eds.), *Mercury: The view after MESSENGER* (pp. 249–286). Cambridge University Press. <https://doi.org/10.1017/9781316650684.011>
- Byrne, P. K., Ostrach, L. R., Fassett, C. I., Chapman, C. R., Denevi, B. W., Evans, A. J., Klimczak, C., Banks, M. E., Head, J. W., & Solomon, S. C. (2016). Widespread effusive volcanism on Mercury likely ended by about 3.5 Ga. *Geophysical Research Letters*, 43(14), 7408–7416. <https://doi.org/10.1002/2016GL069412>
- Cavanaugh, J. F., Smith, J. C., Sun, X., Bartels, A. E., Ramos-Izquierdo, L., Krebs, D. J., McGarry, J. F., Trunzo, R., Novo-Gradac, A. M., Britt, J. L., Karsh, J., Katz, R. B., Lukemire, A. T., Szymkiewicz, R., Berry, D. L., Swinski, J. P., Neumann, G. A., Zuber, M. T., & Smith, D. E. (2007). The Mercury laser altimeter instrument for the MESSENGER mission. *Space Science Reviews*, 131(1–4), 451–479. <https://doi.org/10.1007/s11214-007-9273-4>
- Daniels, J. W., & Neish, C. D. (2018). Impact Melt Emplacement on Mercury. The University of Western Ontario.
- Davies, M. E., Dwornik, S. E., Gault, D. E., & Strom, R. G. (1978). Atlas of Mercury.
- DeHon, R. A., Scott, D. H., & Underwood, J. R. (1981). Geologic Map of the Kuiper Quadrangle of Mercury.
- Denevi, B. W., Chabot, N. L., Murchie, S. L., Becker, K. J., Blewett, D. T., Domingue, D. L., Ernst, C. M., Hash, C. D., Hawkins, S. E., Keller, M. R., Laslo, N. R., Nair, H., Robinson, M. S., Seelos, F. P., Stephens, G. K., Turner, F. S., & Solomon, S. C. (2018). Calibration, projection, and final image products of MESSENGER's Mercury Dual Imaging System. *Space Science Reviews*, 214(1), <https://doi.org/10.1007/s11214-017-0440-y>
- Denevi, B. W., Ernst, C. M., Meyer, H. M., Robinson, M. S., Murchie, S. L., Whitten, J. L., Head, J. W., Watters, T. R., Solomon, S. C., Ostrach, L. R., Chapman, C. R., Byrne, P. K., Klimczak, C., & Peplowski, P. N. (2013). The distribution and origin of smooth plains on Mercury. *Journal of Geophysical Research: Planets*, 118(5), 891–907. <https://doi.org/10.1002/jgre.20075>
- Denevi, B. W., Ernst, C. M., Prockter, L. M., Robinson, M. S., Spudis, P. D., Klima, R. L., Murchie, S. L., Solomon, S. C., Whitten, J. L., Povilaitis, R. Z., & Kinczyk, M. J. (2016). The origin of Mercury's oldest surfaces and the nature of intercrater plains resurfacing. *Lunar and Planetary Science Conference*, 47, 1624.
- Denevi, B. W., Robinson, M. S., Solomon, S. C., Murchie, S. L., Blewett, D. T., Domingue, D. L., McCoy, T. J., Ernst, C. M., Head, J. W., Watters, T. R., & Chabot, N. L. (2009). The evolution of Mercury's crust: A global perspective from MESSENGER. *Science*, 324(5927), 613–618. <https://doi.org/10.1126/science.1172226>
- Denevi, B. W., Seelos, F. P., Ernst, C. M., Keller, M. R., Chabot, N. L., Murchie, S. L., Domingue, D. L., Hash, C. D., & Blewett, D. T. (2016). Final calibration and multispectral map products from the Mercury Dual Imaging System Wide-Angle Camera on MESSENGER. *Lunar and Planetary Science Conference*, 1–2 2016LPI...47.1264D.
- Ernst, C. M., Denevi, B. W., & Ostrach, L. R. (2017). Updated absolute age estimates for the Tolstoj and Caloris basins, Mercury, in: Lunar and Planetary Science Conference. pp. 1–2.
- Fassett, C. I., Head, J. W., Baker, D. M. H., Zuber, M. T., Smith, D. E., Neumann, G. A., Solomon, S. C., Klimczak, C., Strom, R. G., Chapman, C. R., Prockter, L. M., Phillips, R. J., Oberst, J., & Preusker, F. (2012). Large impact basins on Mercury: Global distribution, characteristics, and modification history from MESSENGER orbital data. *Journal of Geophysical Research: Planets*, 117, 1–15. <https://doi.org/10.1029/2012JE004154>
- Fassett, C. I., Head, J. W., Blewett, D. T., Chapman, C. R., Dickson, J. L., Murchie, S. L., Solomon, S. C., & Watters, T. R. (2009). Caloris impact basin: Exterior geomorphology, stratigraphy, morphometry, radial sculpture, and smooth plains deposits. *Earth and Planetary Science Letters*, 285(3–4), 297–308. <https://doi.org/10.1016/j.epsl.2009.05.022>
- Fassett, C. I., Kadish, S. J., Head, J. W., Solomon, S. C., & Strom, R. G. (2011). The global population of large craters on Mercury and comparison with the Moon. *Geophysical Research Letters*, 38, 1–6. <https://doi.org/10.1029/2011GL047294>
- Fegan, E. R. (2018). Crustal History Indicators on Mercury. Crustal history indicators on Mercury.
- Galluzzi, V., Guzzetta, L. G., Ferranti, L., Di Achille, G., Rothery, D. A., & Palumbo, P. (2016). Geology of the Victoria quadrangle (H02), Mercury. *Journal of Maps*, 12, 227–238. <https://doi.org/10.1080/17445647.2016.1193777>
- Galluzzi, V., Rothery, D. A., Giacomini, L., Guzzetta, L. G., El Yazidi, M., Ferranti, L., Lennox, A., Malliband, C. C., Man, B., Massironi, M., Palumbo, P., Pegg, D. L., Tognon, T., & Wright, J. (2021). European Quadrangle Mapping of Mercury: Status Report, in: Planetary Geologic Mappers. p. 7027.
- Giacomini, L., Galluzzi, V., Massironi, M., Ferranti, L., & Palumbo, P. (2022). Geology of the Kuiper quadrangle (H06), Mercury. *Journal of Maps*, 18, 246–257. <https://doi.org/10.1080/17445647.2022.2035268>
- Gillis-Davis, J. J., Blewett, D. T., Gaskell, R. W., Denevi, B. W., Robinson, M. S., Strom, R. G., Solomon, S. C., & Sprague, A. L. (2009). Pit-floor craters on Mercury: Evidence of near-surface igneous activity. *Earth and Planetary Science Letters*, 285(3–4), 243–250. <https://doi.org/10.1016/j.epsl.2009.05.023>
- Goudge, T. A., Head, J. W., Kerber, L., Blewett, D. T., Denevi, B. W., Domingue, D. L., Gillis-Davis, J. J., Gwinner, K., Helbert, J., Holsclaw, G. M., Izenberg, N. R., Klima, R. L., McClintock, W. E., Murchie, S. L., Neumann, G. A., Smith, D. E., Strom, R. G., Xiao, Z., Zuber, M. T., ... Solomon, S. C. (2014). Global inventory and characterization of pyroclastic deposits on Mercury: New insights into pyroclastic activity from MESSENGER orbital data. *Journal of Geophysical Research: Planets*, 119(3), 635–658. <https://doi.org/10.1002/2013JE004480>
- Grolier, M. J., & Boyce, J. M. (1984). Geologic map of the Borealis region (H-1) of Mercury. USGS Miscellaneous Investigations Series Map I-1660 1–1.
- Guest, J. E., & Greeley, R. (1983). Geologic Map of the Shakespeare Quadrangle of Mercury.
- Guzzetta, L. G., Galluzzi, V., Ferranti, L., & Palumbo, P. (2017). Geology of the Shakespeare quadrangle (H03), Mercury. *Journal of Maps*, 13, 227–238. <https://doi.org/10.1080/17445647.2017.1290556>
- Hauber, E., Naß, A., Skinner, J. A., & Huff, A. (2020). Planetary Geologic Mapping. https://doi.org/10.1007/978-3-319-62849-3_5

- Hawkins, S. E., Boldt, J. D., Darlington, E. H., Espiritu, R., Gold, R. E., Gotwols, B., Grey, M. P., Hash, C. D., Hayes, J. R., Jaskulek, S. E., Kardian, C. J., Keller, M. R., Malaret, E. R., Murchie, S. L., Murphy, P. K., Peacock, K., Prockter, L. M., Reiter, R. A., Robinson, M. S., ... Williams, B. D. (2007). The Mercury Dual Imaging System on the MESSENGER spacecraft. *Space Science Reviews*, 131(1-4), 247–338. <https://doi.org/10.1007/s11214-007-9266-3>
- Howe, R. C. (1997). Geologic contacts. *Journal of Geoscience Education*, 45(2), 133–136. <https://doi.org/10.5408/1089-9995-45.2.133>
- Hynek, B. M., Robbins, S. J., Muller, K., Gemperline, J., & Osterloo, M. K. (2017). Unlocking Mercury's geological history with detailed mapping of Rembrandt basin: Year 3. 3rd Planetary Data Workshop 2017 3, 7089.
- Jozwiak, L. M., Head, J. W., & Wilson, L. (2018). Explosive volcanism on Mercury: Analysis of vent and deposit morphology and modes of eruption. *Icarus*, 302, 191–212. <https://doi.org/10.1016/j.icarus.2017.11.011>
- Kennedy, M., & Kopp, S. (2004). Understanding Map Projections GIS by ESRI, in: GIS by ESRI. Environmental Systems Research Institute, Inc., pp. 1–116.
- Kerber, L., Head, J. W., Blewett, D. T., Solomon, S. C., Wilson, L., Murchie, S. L., Robinson, M. S., Denevi, B. W., & Domingue, D. L. (2011). The global distribution of pyroclastic deposits on Mercury: The view from MESSENGER flybys 13. *Planetary and Space Science*, 59(15), 1895–1909. <https://doi.org/10.1016/j.pss.2011.03.020>
- Kinczyk, M. J., Prockter, L. M., Byrne, P. K., Denevi, B. W., Buczkowski, D. L., Ostrach, L. R., & Miller, E. B. (2019). The first global geological map of Mercury. *EPSC-DPS Joint Meeting*, 13, 1045.
- Kinczyk, M. J., Prockter, L. M., Byrne, P. K., Susorney, H. C. M., & Chapman, C. R. (2020). A morphological evaluation of crater degradation on Mercury: Revisiting crater classification with MESSENGER data. *Icarus*, 341, 113637. <https://doi.org/10.1016/j.icarus.2020.113637>
- King, J. S., & Scott, D. H. (1990). Geologic Map of the Beethoven Quadrangle of Mercury.
- Klimczak, C., Byrne, P. K., Sengör, A. M. C., & Solomon, S. C. (2019). Principles of structural geology on rocky planets. *Canadian Journal of Earth Sciences*, 56(12), 1437–1457. <https://doi.org/10.1139/cjes-2019-0065>
- Leake, M. A. (1981). The Intercrater Plains Of Mercury And The Moon: Their Nature, Origin, And Role In Terrestrial Planet Evolution.
- Malliband, C. C., Rothery, D. A., Balme, M. R., Conway, S. J., Pegg, D. L., & Wright, J. (2023). Geology of the Derain quadrangle (H10), Mercury. *Journal of Maps*, 1–10. <https://doi.org/10.1080/17445647.2022.2112774>
- Mancinelli, P., Minelli, F., Pauselli, C., & Federico, C. (2016). Geology of the Raditladi quadrangle, Mercury (H04). *Journal of Maps*, 12, 190–202. <https://doi.org/10.1080/17445647.2016.1191384>
- Marchi, S., Chapman, C. R., Fassett, C. I., Head, J. W., Bottke, W. F., & Strom, R. G. (2013). Global resurfacing of Mercury 4.0–4.1 billion years ago by heavy bombardment and volcanism. *Nature*, 499(7456), 59–61. <https://doi.org/10.1038/nature12280>
- McGill, G. E., & King, E. A. (1983). Geologic Map of the Victoria Quadrangle of Mercury.
- Murchie, S. L., Mick, A., Prockter, L. M., Rivkin, A., Guinness, E., & Ward, J. (2017). MDIS CDR / RDR SOFTWARE INTERFACE SPECIFICATION.
- Neish, C. D., Blewett, D. T., Harmon, J. K., Coman, E. I., Cahill, J. T. S., & Ernst, C. M. (2013). A comparison of rayed craters on the Moon and Mercury. *Journal of Geophysical Research: Planets*, 118(10), 2247–2261. <https://doi.org/10.1002/jgre.20166>
- Pegg, D. L., Rothery, D. A., Balme, M. R., & Conway, S. J. (2021a). Explosive vent sites on Mercury: Commonplace multiple eruptions and their implications. *Icarus*, 365, 114510. <https://doi.org/10.1016/j.icarus.2021.114510>
- Pegg, D. L., Rothery, D. A., Balme, M. R., Conway, S. J., Malliband, C. C., & Man, B. (2021b). Geology of the Debussy quadrangle (H14), Mercury. *Journal of Maps*, 17, 718–729. <https://doi.org/10.1080/17445647.2021.1996478>
- Prockter, L. M., Kinczyk, M. J., Byrne, P. K., Denevi, B. W., Head, J. W., Fassett, C. I., Whitten, J. L., Thomas, R. J., Buczkowski, D. L., Hynek, B. M., Ostrach, L. R., Blewett, D. T., & Ernst, C. M. (2012). The first global Map of Mercury, In: Lunar and planetary science conference. pp. 1–2. <https://doi.org/10.1029/2012JE004154>
- Rothery, D. A., Thomas, R. J., & Kerber, L. (2014). Prolonged eruptive history of a compound volcano on Mercury: Volcanic and tectonic implications. *Earth and Planetary Science Letters*, 385, 59–67. <https://doi.org/10.1016/j.epsl.2013.10.023>
- Schaber, G. G., & McCauley, J. F. (1980). Geologic Map of the Tolstoj Quadrangle of Mercury.
- Semenzato, A., Massironi, M., Ferrari, S., Galluzzi, V., Rothery, D. A., Pegg, D. L., Pozzobon, R., & Marchi, S. (2020). An integrated geologic map of the Rembrandt basin, on Mercury, as a starting point for stratigraphic analysis. *Remote Sensing*, 12(19), 3213–3233. <https://doi.org/10.3390/rs12193213>
- Skinner, J. A., Huff, A. E., Black, S. R., Buban, H. C., Fortezzo, C. M., Gaither, T. A., Hare, T. M., & Hunter, M. A. (2022). Planetary Geologic Mapping Protocol — 2022: U.S. Geological Survey Techniques and Methods 11-B13.
- Solomon, S. C., & Anderson, B. J. (2018). The MESSENGER mission: Science and implementation overview, in: Mercury. Cambridge University Press, pp. 1–29.
- Spudis, P. D., & Guest, J. E. (1988). Stratigraphy and geologic history of Mercury. *Mercury*, 118–164.
- Spudis, P. D., & Prosser, J. G. (1984). Geologic Map of the Michelangelo Quadrangle of Mercury.
- Strom, R. G. (1977). Origin and relative age of Lunar and Mercurian intercrater plains. *Physics of the Earth and Planetary Interiors*, 15(2-3), 156–172. [https://doi.org/10.1016/0031-9201\(77\)90028-0](https://doi.org/10.1016/0031-9201(77)90028-0)
- Strom, R. G., Malin, M. C., Leake, M. A., & Kozak, R. (1990). Geologic Map Of The Bach (H-15) Quadrangle.
- Strom, R. G., Trask, N. J., & Guest, J. E. (1975). Tectonism and volcanism on Mercury. *Journal of Geophysical Research*, 80(17), 2478–2507. <https://doi.org/10.1029/JB080i017p02478>
- Thomas, R. J., & Rothery, D. A. (1984). Volcanism on Mercury. *Bulletin Volcanologique*, 47, 531–535. <https://doi.org/10.1007/BF01961224>
- Thomas, R. J., Rothery, D. A., Conway, S. J., & Anand, M. (2014a). Hollows on Mercury: Materials and mechanisms involved in their formation. *Icarus*, 229, 221–235. <https://doi.org/10.1016/j.icarus.2013.11.018>
- Thomas, R. J., Rothery, D. A., Conway, S. J., & Anand, M. (2014b). Long-lived explosive volcanism on Mercury. *Geophysical Research Letters*, 41(17), 6084–6092. <https://doi.org/10.1002/2014GL061224>
- Thomas, R. J., Rothery, D. A., Conway, S. J., & Anand, M. (2014c). Mechanisms of explosive volcanism on

- Mercury: Implications from its global distribution and morphology. *Journal of Geophysical Research: Planets*, 119(10), 2239–2254. <https://doi.org/10.1002/2014JE004692>
- Tobler, W. (1987). Measuring spatial resolution. *Land Resources Information Systems Conference*, 12–16.
- Trask, N. J., & Dzurisin, D. (1984). Geologic Map of the Discovery Quadrangle of Mercury.
- Trask, N. J., & Guest, J. E. (1975). Preliminary geologic terrain map of Mercury. *Journal of Geophysical Research*, 80(17), 2461–2477. <https://doi.org/10.1029/JB080i017p02461>
- Watters, T. R., Head, J. W., Solomon, S. C., Robinson, M. S., Chapman, C. R., Denevi, B. W., Fassett, C. I., Murchie, S. L., & Strom, R. G. (2009). Evolution of the Rembrandt impact basin on Mercury. *Science*, 324(5927), 618–621. <https://doi.org/10.1126/science.1172109>
- Whitten, J. L., & Head, J. W. (2015). Rembrandt impact basin: Distinguishing between volcanic and impact-produced plains on Mercury. *Icarus*, 258, 350–365. <https://doi.org/10.1016/j.icarus.2015.06.022>
- Whitten, J. L., Head, J. W., Denevi, B. W., & Solomon, S. C. (2014). Intercrater plains on Mercury: Insights into unit definition, characterization, and origin from MESSENGER datasets. *Icarus*. <https://doi.org/10.1016/j.icarus.2014.06.013>
- Wood, C. A., Head, J. W., & Cintala, M. J. (1977). Crater degradation on Mercury and the Moon: Clues to surface evolution, In: Proc. Lunar Sci. Conf. 8th. pp. 3503–3520.
- Wright, J., Rothery, D. A., Balme, M. R., & Conway, S. J. (2019). Geology of the Hokusai quadrangle (H05), Mercury. *Journal of Maps*, 15, 509–520. <https://doi.org/10.1080/17445647.2019.1625821>
- Xiao, Z., Xu, R., Wang, Y., Chang, Y., Xu, R., & Cui, J. (2021). Recent dark pyroclastic deposits on Mercury. *Geophysical Research Letters*, 48, 1–11. <https://doi.org/10.1029/2021GL092532>